

# Methodologies for Successful Segmentation of HRTEM Images via Neural Network

Catherine K. Groschner and Christina Choi  
*Department of Materials Science and Engineering,  
 University of California Berkeley, Berkeley, CA 94720*

M. C. Scott<sup>\*</sup>  
*Department of Materials Science and Engineering,  
 University of California Berkeley, Berkeley, CA 94720 and  
 Molecular Foundry, Lawrence Berkeley National Laboratory, Berkeley, CA 94720<sup>†</sup>*

High throughput analysis of samples has been a topic increasingly discussed in both light and electron microscopy. Deep learning can help implement high throughput analysis by segmenting images in a pixel-by-pixel fashion and classifying these regions. However, to date, relatively little has been done in the realm of automated high resolution transmission electron microscopy (HRTEM) micrograph analysis. Neural networks for HRTEM have, so far, focused on identification of single atomic columns in single materials systems. For true high throughput analysis, networks will need to not only recognize atomic columns but also segment out regions of interest from background for a wide variety of materials. We therefore analyze the requirements for achieving a high performance convolutional neural network for segmentation of nanoparticle regions from amorphous carbon in HRTEM images. We also examine how to achieve generalizability of the neural network to a range of materials. We find that networks trained on micrographs of a single material system result in worse segmentation outcomes than one which is trained on a variety of materials' micrographs. Our final network is able to segment nanoparticle regions from amorphous background with 91% pixelwise accuracy.

## I. INTRODUCTION

The last decade has seen a huge push in high throughput materials discovery. A portion of this has been the Materials Project, which provides high throughput computations of material properties [1]. Similarly, other high throughput materials discovery efforts have also created a need for automated structural validation which can be used in a high throughput manner [2–4]. This is particularly apparent in the area of high throughput nanomaterial design and synthesis, where microstructural features, such as nanoparticle size and shape or the presence of grain boundaries and crystal defects, can strongly influence the material's properties [5–8]. Additionally, heterogeneity in these microstructural features within populations of nanomaterials will have observable effects on the bulk behavior [6, 7, 9]. Therefore, a means of automated atomic structure characterization is required to complete the high throughput materials discovery process. In addition, one could imagine that automating the atomic resolution segmentation task could be extremely influential in enabling studies of the heterogeneity of nanoparticle populations, an area which has been out of reach.

Electron microscopy is the only technique which can enable the analysis of local atomic-scale structure and account for structural heterogeneity. Techniques such as X-ray diffraction may provide precise crystallographic

information, but only by averaging over the structure of thousands of particles. Electron microscopy is therefore the method of choice to identify local, atomic-scale structural features. However, large scale information extraction from electron micrographs is often prohibitively time consuming. Simple tasks such as particle size and shape classification can be difficult and are often performed manually [10]. While automated identification of local structures is possible [11, 12], it is challenging, time consuming, and sample-dependent, resulting in a constraint on the number of particles and number of samples analyzed. The sample-dependence of previous techniques is a particularly important limitation towards fully automated characterization with HRTEM. Because the sample will determine the amount of scattering and therefore the contrast between nanoparticle and background, methods that rely solely on thresholding may fail unpredictably when broadly applied. Here we demonstrate a method for transferable, automated identification of metallic nanoparticle structures from HRTEM, which relies not only on changes in contrast, but on the high-resolution lattice texture in the nanoparticles themselves. Given recent advances in image interpretation using deep learning [13, 14], segmentation *via* convolutional neural net (CNN) is a promising route towards automatic interpretation of HRTEM micrographs.

To date, most work on segmentation of TEM images has been applied to biological samples and cryo-electron microscopy [15, 16]. However, the different length scales involved in these imaging modalities mean that detection can largely revolve around edge detection and be dependent on mass and thickness contrast.

<sup>\*</sup> Corresponding author

<sup>†</sup> [mary.scott@berkeley.edu](mailto:mary.scott@berkeley.edu)

High resolution imaging for materials science samples are dependent on much different contrast mechanisms; predominately phase contrast which can result in highly nonlinear images [17]. Due to the image not being a simple projection of atomic potentials, previously implemented particle detection methods are not expected to be effective.

Only recently has there been work on segmentation of HRTEM and high resolution scanning transmission electron microscopy (HRSTEM). The application of CNNs to HRSTEM data has focused primarily on identifying atoms in sheets of material filling the entire field of view or in the prediction of atomic column thickness or specific atom tracking [18–23]. Most work in this area has focused on atomic column finding in HRSTEM images, for example atom finding on large graphene sheets in HRSTEM data to identify defects [18] [20]. This approach has also been applied to HRSTEM *in situ* movies of WS<sub>2</sub> [21]. While most of these works focus on a thin film which fills the field of view, recent work has identified atomic columns belonging to a graphene region surrounded by amorphous carbon [24]. Less work has been done in the area of HRTEM but what has been done has also focused on atomic column finding, with applications in strain and thickness measurement [19]. Particle finding algorithms have been implemented, but have not been sensitive to local atomic structure [25], and the issue of generalizability has not been addressed.

We have focused on HRTEM as opposed to HRSTEM as it is a more dose-efficient imaging mode and therefore useful for a wider range of materials. However, segmentation in HRTEM is particularly challenging because the contrast between the substrate that the nanomaterial sits on and the nanomaterial itself can be very low. Because traditional image processing techniques are highly error prone for these types of images, we have implemented a convolutional neural network to handle semantic segmentation, which is segmentation of the image on a pixel by pixel basis. Neural network based semantic segmentation has the added benefit of giving a confidence of prediction for each pixel. We are particularly interested in segmenting out nanoparticle regions as opposed to individual atomic columns because then larger structural features and relationships between atomic columns can be analyzed on a particle by particle basis. For example, these segmented regions can then be passed to other classifiers and techniques for various structural analysis such as classifying nanoparticles containing dislocations. We use CNNs specifically because they have the flexibility to generalize across samples and the speed to be used in other methods such as *in-situ* particle tracking.

Here we present a solution to nanoparticle region identification in HRTEM that performs well on nanoparticles with a wide range of compositions and therefore scattering intensities. We have explored the impact of training set on segmentation by analyzing the results of three separately trained networks. We

have found that networks trained only on micrographs of highly scattering samples or lightly scattering samples are not as robust as those which see a more diverse dataset. We show that the more diverse dataset increases pixelwise segmentation accuracy and dice coefficient for each individual dataset over networks trained to each specific dataset. These results point to a means of achieving segmentation on a wide variety of nanoparticle samples. This is likely due to the sensitivity of the neural network to lattice features. Our best performing CNN is able to segment nanoparticles with a 91% pixelwise accuracy. We were able to train this neural network using only 129 512x512 micrographs through data augmentation. The neural network is shown to be robust to changes in contrast and is sensitive to the presence of atomic columns. We confirm this atomic column sensitivity by analyzing the activation maps from the neural network. Taken as a whole, this represents a critical step to an automated imaging, particle identification, and structure analysis workflow for nanoparticles.

## II. METHODS

The overall goal of this work was to achieve accurate segmentation on micrographs of 2 nm CdSe nanoparticles. These samples were particularly challenging because of the relatively low electron scattering from the low atomic number sample. Datasets of CdSe nanoparticles and Au nanoparticles were acquired in order to test the neural network’s sensitivity to changes in contrast, due to the change in scattering potential of the different materials. CdSe micrographs provided a low scattering potential case while the Au nanoparticles were in the high scattering potential regime. Three separate neural networks were trained. The first was trained using only Au data, the second using only CdSe data, and the third was trained using a combination of both. Each time the network was only trained using 129 images in total. These three cases allowed us to test whether training would be more successful on narrower tasks, such as identifying a single material, or whether a greater diversity of images would improve results. Micrographs of a completely different material system, Pd nanoparticles, were not used in training but were used to test the generalizability of the network to different materials.

### A. Sample Preparation and Data Collection

We collected CdSe micrographs using the TEAM 0.5 aberration corrected microscope at an operating voltage of 300 kV. CdSe particles were synthesized via the WANDA synthesis robot at the Molecular Foundry [5]. This solution was then diluted with hexane and dropcast on 200 mesh ultra-thin carbon grids. Forty six 1024x1024

images were taken by hand. Labels for this dataset were manually created using the MATLAB labeler app [26]. The CdSe particles being smaller and a lower atomic number material provided a lower contrast and, therefore, lower signal to background dataset.

Au nanoparticle data was collected using an FEI Themis with image aberration correction operated at 300 kV. Au nanoparticles in phosphate buffered saline were purchased from Sigma Aldrich. The Au nanoparticle solution was diluted with water and dropcast on to 200 mesh carbon grids. Prior to drop casting, carbon grids were cleaned using a plasma cleaner. Thirteen 4026x4026 TEM micrographs were collected using SerialEM. SerialEM is a software which enables automated electron microscopy imaging [27], and was used for automated focusing in order to speed up image collection. The autofocus function also helped ensure that the range of defocus was within approximately 100 nm of Gaussian focus. Labels for network training were created by hand using the MATLAB labeler application [26].

Palladium nanoparticles were synthesized by a solution method developed by Lim *et al.* [28]. 2  $\mu$ L of the purified solution was then dropcast onto a 200 mesh carbon grid. Prior to dropcasting the carbon grids were cleaned using a plasma cleaner. The nanoparticles were then imaged using a FEI Themis with image aberration correction operated at 300kV.

## B. Data Preprocessing

After data collection, there were several key steps in data preprocessing. For the segmentation, two classes were used: the nanoparticle class and the background class. Any contiguous crystalline region was labelled as being part of the nanoparticle class. All other regions were labelled as carbon background. Should there have been contamination a third class would have been needed, but in this case clean enough samples were prepared for this to not be necessary.

Images collected were 4096x4096 or 1024x1024 in Int16 format. Since large images make segmentation significantly more computationally demanding, we sliced each image and its ground truth segmentation map into 512x512 images which remained in Int16 format. Keeping data in Int16 format was found to be crucial as converting to Int8 (as would be found in standard pngs) negatively impacted network training due to the limited the dynamic range typical of HRTEM images. We used the openNCEM Python package in combination with custom code to for the image preprocessing [29]. OpenNCEM was used for reading the mrc files produced by the microscope software into Python. Opened mrc files were then matched with the png label files so that both could be put into numpy arrays and saved as h5 files. Once data had been properly sorted, both images and labels were sliced into 512x512 chunks and put into

an array. All the images were then normalized by first applying a median filter with a 3x3 kernel which served to remove spurious X-rays. After filtering, the images were normalized by the filtered dataset maximum.

Significant portions of the raw input images were carbon background, which meant that when sliced into 512x512 images only 28% of images contained nanoparticles. Since a class must be predicted for each pixel, having only 28% of images contain particles meant that the background class was drastically over represented in the training, validation, and test set [30]. Therefore, we implemented a rough balancing of classes by using the ground truth segmentation maps to determine which 512x512 images contained any pixels belonging to the particle class. Any image that did not contain particle class pixels was discarded from the training and test set. For each network, 97 images were used in the training set, 32 images were in the validation set, and 46 images were in the test set.

## C. Network Training

For this experiment, three separate neural networks were trained. One was trained solely on Au nanoparticle data, while the second was trained only on CdSe data. The third was trained on a combination of Au and CdSe data. The number of images used for training remained consistent for all three networks.

Processed micrographs were fed to a Keras image augmentation generator [31]. The architecture implemented was based on the U-Net architecture developed by Ronneberger *et al* following the same convolution-deconvolution structure [14]. We, however, implemented our neural network with much shallower features and several more convolutional and deconvolutional layers. Figure 1 explains the architecture we used. We also included dropout, a layer which randomly removes a certain portion of features, which Ronneberger did not. Most of these deviations from the original paper were to prevent overfitting. We found that a lighter architecture performed better than the original architecture described by Ronneberger *et al.* Whereas the original U-Net went from 572x572 with a depth of 1 to 28x28 with a depth of 1024, we found that neither this reduction in size nor number of features is necessary. Our network has an input of 512x512 with depth 1 (grayscale image) and has the smallest feature of 32x32 with a depth of 32. The network was trained to segment all crystalline regions from the non-crystalline background.

Training was performed using the Savio GPU cluster at U.C. Berkeley using a compute node with two Intel Xeon E5-2623 v3 CPU cores and an NVIDIA K80 GPU. The node had 64 GB of available RAM. The model was built using Keras with a Tensorflow backend [31]. Training used 97 sample images, which then fed into an image generator, which randomly rotated and

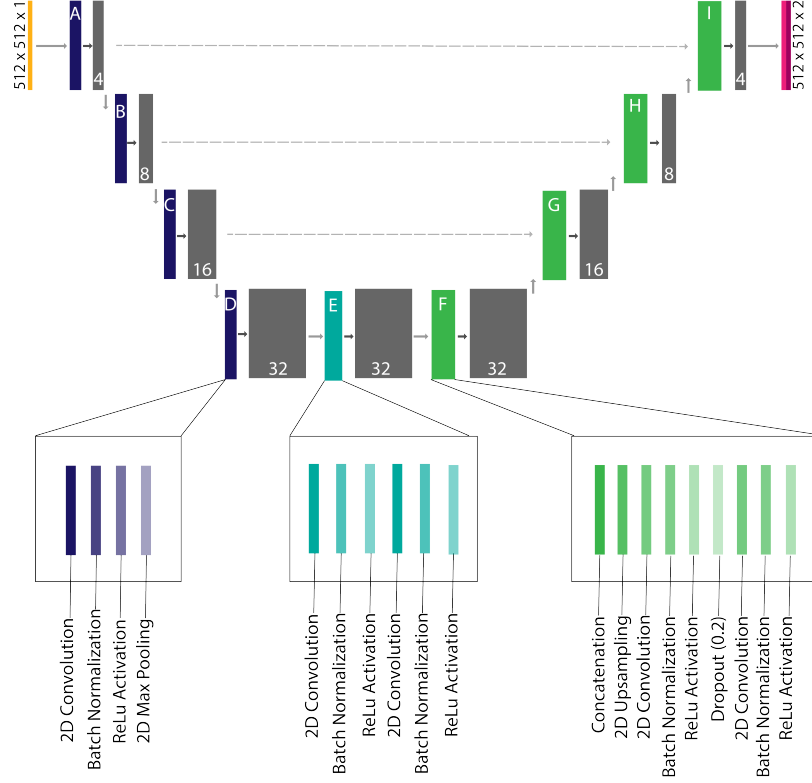


FIG. 1. The U-Net style architecture of CNN implemented for segmentation of nanoparticle regions. Layers colored gray represent the output features and are labeled with the number of features created. Layers A-D contain a 2D convolutional layer, batch normalization layer, ReLu activation layer, and a 2D max pooling layer. Layer E contains a 2D convolutional layer, batch normalization layer, and ReLu activation layer, which is repeated once. Layers F-I contain a 2D upsampling layer, concatenation layer, a 2D convolution, batch normalization, and ReLu activation followed by a dropout layer and another set of 2D convolution, batch normalization, and ReLu activation layers. The final layer is a sigmoid activation layer which outputs two segmentation maps one for each class, background and particle.

flipped the images. The only augmentations allowed were rotations from 0-360 degrees, and mirroring. Each epoch contained 1,000 samples created from rotating the original processed 97 micrographs. Early stopping was implemented such that validation loss did not improve more than 0.001 after two epochs. The model was limited to train for a maximum of ten epochs. The model used categorical cross entropy for the loss function and Adam as the optimizer with a learning rate was  $1 \times 10^{-4}$  [32, 33]. Batch size was set to 20. The model was updated based on the results of a validation set containing 32 images. Training was done independently for each different dataset.

#### D. Multiclass to Binary Classification

Despite only having two classes, we chose to treat this problem as a multiclass classification problem. Instead of having the neural network output a single segmentation map, which classifies the particle regions as 1 and the background as 0, we have it predict a segmentation map for both the background and particle class, as can be

seen in the final output shown in Figure 1. We found that this lead to better learning of the background class and therefore better end segmentation. This was evident by the decrease in the number of false positives when the neural network predicted two separate segmentation maps, one for each class.

Since the output of the neural network is two separate segmentation maps, we must choose one for the final segmentation of pixels. For most training instances, the segmentation map for the particle class was more confident in its predictions for each pixel and yielded higher accuracy. Therefore, the final segmentation maps were based on thresholding the particle segmentation map. The threshold was set to optimize pixelwise accuracy on the training data.

#### E. Testing

A holdout test dataset was reserved for final testing after model training had completed. This test set is separate from the validation set used during training. It consisted of 46 images. The model predicted



segmentation maps for both the background and particle class of the test set. The final segmentation map was then taken from the particle segmentation map, which was then thresholded based on the previously determined threshold, as described above. Pixelwise accuracy values and dice coefficients were then calculated based on these thresholded segmentation maps.

### III. RESULTS AND DISCUSSION

We tested whether networks trained on the same nanoparticle material datasets could perform better on their specific dataset than on a network which had been trained on a combination dataset. This was to test whether networks would need to be trained for individual material cases. Sample materials were hypothesized to influence neural network performance due to the dependence of image contrast on the scattering potential of the material. Overall, we found that a more diverse feature space created by training on a combination dataset actually improved segmentation results for both the Au and CdSe datasets. Finally, we also tested the generalizability of the combination network by having it segment a micrograph of Pd allowing us to test how the network responded on a new material system, under a variety of imaging conditions.

#### A. Results from Training with Gold Nanoparticle Micrographs

The first network was trained only on the Au nanoparticle dataset. This network had good performance on the Au nanoparticle test set. It achieved a dice coefficient of 0.79 and a pixelwise accuracy of 88% on the test set. Figure 2a and b show a sample Au nanoparticle micrograph from the test set and the network's segmentation. From the sample image, it is clear that the network provides good segmentation on the nanoparticle region with strong atomic column contrast. However, there is obvious failure in regions where the atomic columns are not as clearly defined. Figure 2c presents the confusion matrix for of the network on a sample. From the confusion matrix, it is clear that the background pixels are segmented with high accuracy. However, as was shown from the sample micrograph, the network struggles with false negatives and therefore much of the background accuracy is due to overpredicting the background class.

While the network trained only on Au nanoparticle micrographs performed fairly well on the Au nanoparticle test set, it also needed to be tested for generalizability. Therefore a test set of CdSe micrographs was used to see how it would handle this lower scattering case. However, when tested on the CdSe dataset, the network fails dramatically. This can be seen in the confusion matrix presented in Figure 2f, which shows that the

network essentially defaults to classifying all the pixel regions as particle pixels. This is also reflected in the segmentation map in 2e, where there are a significant number of false positives. While this result is not entirely unexpected given that the neural network was not trained on the CdSe set, it does suggest that the network lacks generalizability and is learning features specifically to the higher contrast Au nanoparticle dataset.

#### B. Results from Training with CdSe Nanoparticle Micrographs

A material-specific network was tested for segmentation of the CdSe dataset. This network was trained on a subset of the CdSe data. The resulting network had a pixelwise accuracy of 87% but a dice coefficient of only 0.24. The confusion matrix of this test are shown in Figure 3c. Clearly, the features of the nanoparticles in this case are not learned as well as the previous network. Only 14% of particle pixels are correctly classified. This is exemplified in 3a and b which shows several CdSe particles which have been incorrectly labelled. Likely, this is partially due to the number of pixels belonging to each class between the Au nanoparticle and CdSe nanoparticle datasets; 33% of pixels in the Au dataset belonged to the particle class while only 12% of pixels belonged to the particle class in the CdSe dataset. It should be noted that the network was able to successfully recognize some nanoparticle regions. Overall, however, the CdSe only neural network is characterized by a large number of false negatives, suggesting that it learned fewer relevant features for the lower scattering case.

#### C. Results from Training with Combined Dataset

Performance of the Au nanoparticle network was markedly better than the CdSe only network. However, only the CdSe network was able to recognize CdSe regions. Therefore, we hypothesized that training on a combined dataset could serve to learn more robust features for micrographs of samples with large and small scattering factors. A new network was trained on 97 images which were a randomized combination of Au nanoparticle micrographs and CdSe nanoparticle micrographs from the previous training sets. The original separate test sets were then used for each material - the original Au nanoparticle test set and the original CdSe nanoparticle test set. Both sets showed dramatic improvement in performance over the individually trained networks as can be seen in Figure 4, which shows the confusion matrix for each dataset. Both confusion matrices show improved performance in terms of much higher fraction of true positives for both the Au and CdSe datasets. This improved performance is also reflected in the dice coefficient for

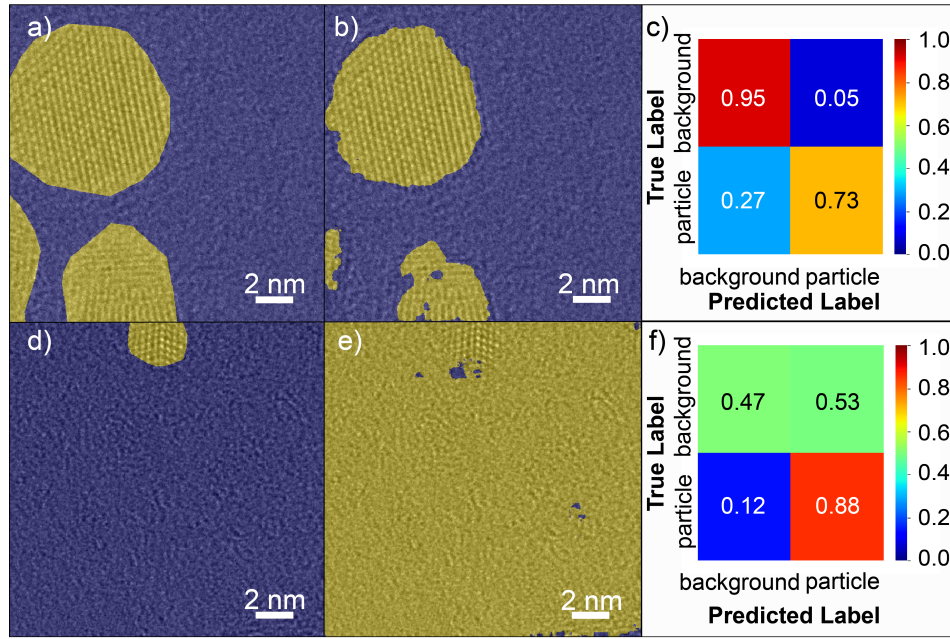


FIG. 2. Results from the network trained only on the Au nanoparticle dataset. a) Sample micrograph of Au nanoparticles with true segmentation map overlaid. b) The resulting segmentation map predicted by the neural network for the sample micrograph. c) The confusion matrix as calculated from the test set of Au nanoparticle micrographs. The top left and bottom right give the fraction of background and particle pixels from the Au nanoparticle test set correctly classified. The top right and bottom left give the fraction of misclassified pixels. d) A sample micrograph of CdSe nanoparticles with true segmentation map overlaid. e) The segmentation map predicted by the neural network trained only on Au nanoparticles. f) The confusion matrix calculated on the CdSe test set. For all segmentation maps, yellow represents regions predicted to be in the particle class, blue regions predicted as background.

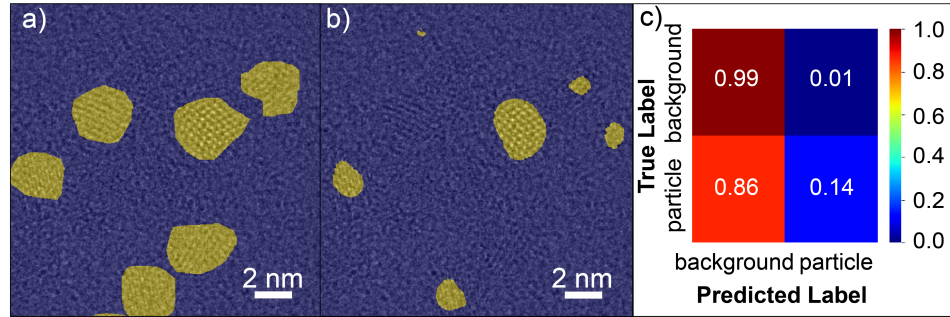


FIG. 3. Results from the network trained only on the CdSe nanoparticle dataset. a) Sample micrograph of CdSe nanoparticles. b) The resulting segmentation map predicted by the neural network for the sample micrograph. c) The confusion matrix as calculated from the test set of CdSe nanoparticle micrographs. The top left and bottom right give the fraction of background and particle pixels from the CdSe nanoparticle test set correctly classified. The top right and bottom left give the fraction of misclassified pixels. For all segmentation maps, yellow represents regions predicted to be in the particle class, blue regions predicted as background.

each dataset. The network achieved a dice coefficient of 0.87 and 92% pixelwise accuracy on the Au dataset, and a dice coefficient of 0.56 and pixelwise accuracy of 89% on the CdSe dataset, significant gains compared to the networks which were individually trained for each network. This suggests that for maximum network efficacy the network should be trained on a diverse range of material datasets. To further test the generalizability of the network, we tested it on a completely new material.

Given a Pd micrograph, the network segmented the nanoparticle with a 96% pixelwise accuracy. The Pd sample segmentation is shown in Figure 5e. The fact that the network was able to generalize onto a new dataset suggests that it is learning generalizable features and not overtraining to the two original datasets.

We next analyzed whether the network would perform at least as well, or better, than traditional threshold based segmentation methods. Therefore, we compared

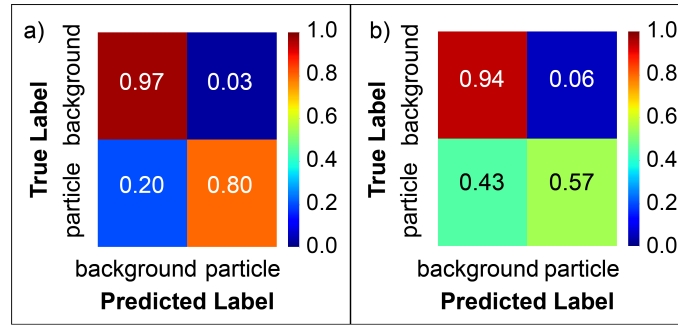


FIG. 4. The confusion matrix from the combined dataset network when applied to Au and CdSe particles respectively. a) Confusion matrix for the Au dataset using the combined dataset network. b) Confusion matrix for the CdSe dataset using the combined dataset network.

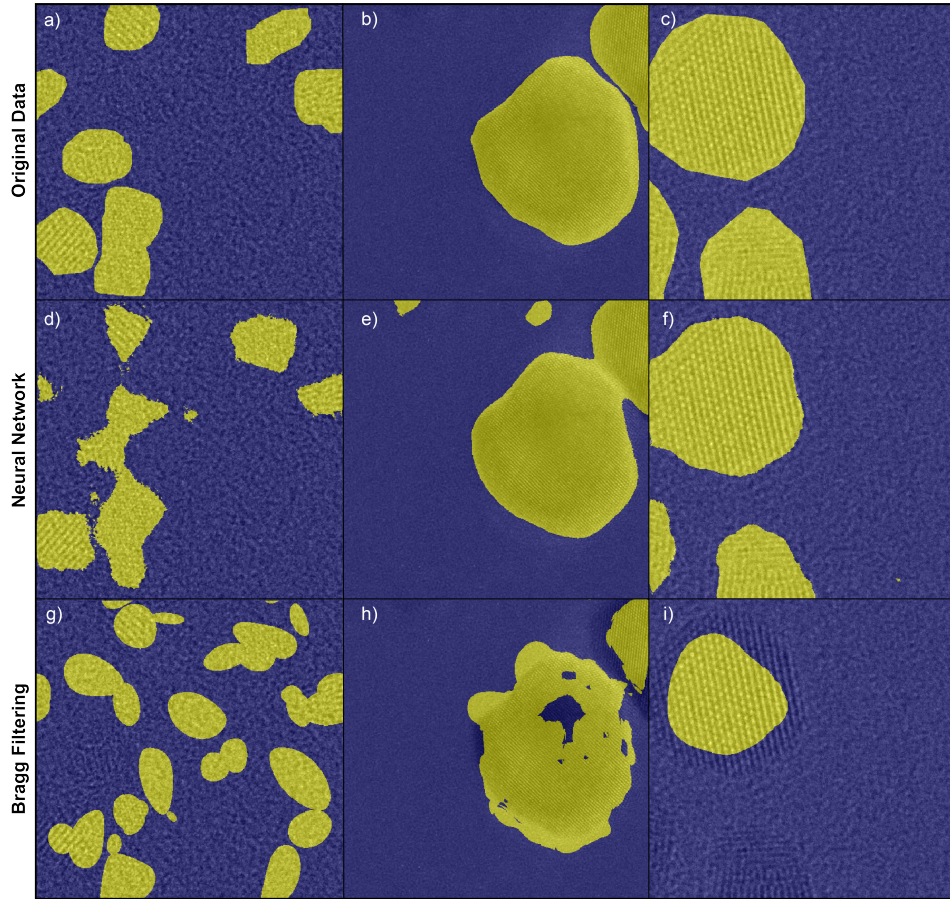


FIG. 5. The top row, a-c, of the figure shows sample images from the CdSe, Pd, and Au datasets from left to right. The second row, d-f, shows segmentation maps for each of the images in the first row generated by the network trained on a combination of CdSe and Au data. The third row, g-i, shows the segmentation maps for the same images that were generated by Bragg peak filtering. For all segmentation maps, yellow represents regions predicted to be in the particle class, blue regions predicted as background.

segmentation by Bragg peak filtering to the results from the neural network for three test images from the three datasets. To Bragg filter images, we first median filtered the intensity of the Fourier transform of each of the three images. This median filtered version of the Fourier transform was then subtracted off the intensity

of the original Fourier transform in order to eliminate background effects and Thon rings. We used convolution and thresholding to locate the Bragg peaks and create a segmented version of Fourier space containing only the Bragg peaks. By applying the inverse Fourier transform a segmentation map was then generated. The results of



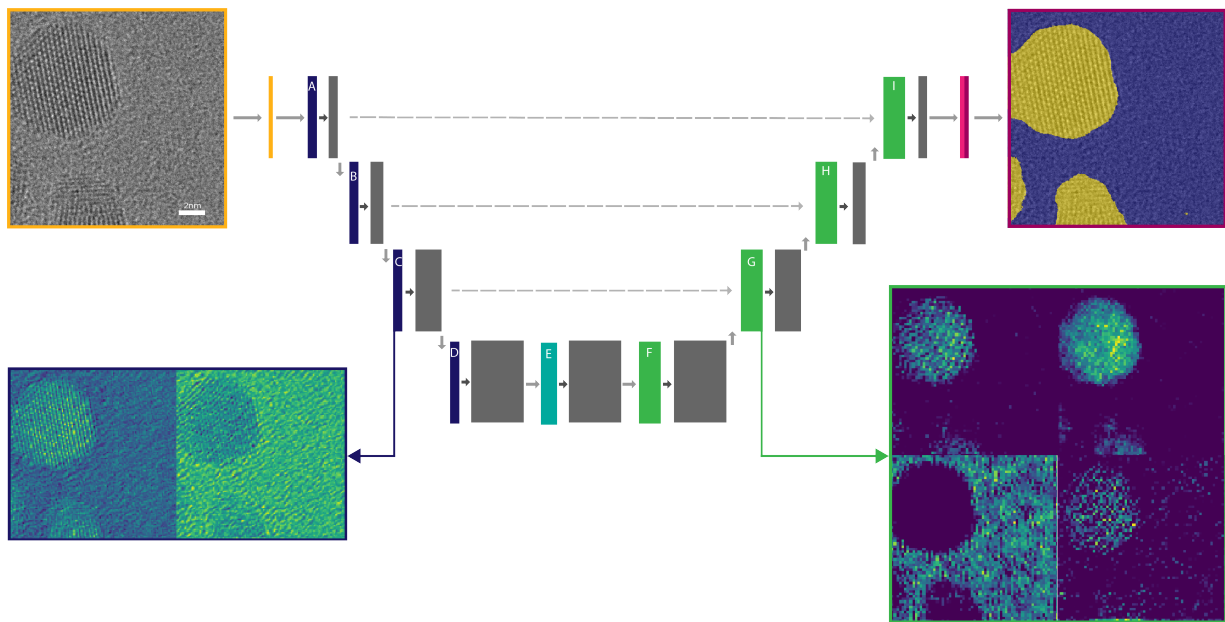


FIG. 6. The neural network architecture showing selected activation maps from various points in the network. The activations on the left show the activations after an early convolutional layer. Activations on the right come from the first concatenation layer.

this method are shown in Figure 5 g-i. From the Bragg peak-based segmentation maps, pixelwise accuracy was calculated for each sample image. CdSe was segmented with 71% accuracy, Pd with 91% accuracy, and Au with 77% accuracy. In comparison, the results for the neural network on these images was a pixelwise accuracy of 88% for CdSe, 96% for Pd, and 94% for Au. The results for Au and Pd were reasonably close between Bragg filtering and the neural network, however the neural network performed much better than the Bragg filtering on the more weakly scattering CdSe. This is due to the Bragg peaks being closer to background for the CdSe images. This resulted in significantly more false positives in Bragg peak identification and therefore the large number of false positive regions. It should also be noted that for reasonably good results for the Bragg filtering case, the thresholding parameters had to be tuned for each individual image, in contrast to the neural network. The neural network required no tuning to the individual micrograph and was successful in its segmentation task immediately for all three sample types. This highlights the truly automated nature of CNN-based segmentation.

The better segmentation for Au nanoparticles, by the neural network trained on mixed data, may be tied to the way in which the network learns the features of the different classes. In order to understand what features the neural network is sensitive to, we analyzed the activations from each layer. The activations shown early in the network in Figure 6 suggest that in the beginning the network is learning differences between particle and background features. This is seen by looking at which regions are highlighted in the activations relative to

the image. The later activations show highlighting of specific atomic columns, suggesting the network is actually learning to distinguish the actual atomic column features. Looking back at the results from the Au trained neural network in Figure 2b, it can be seen that some of the lattice features are missed in the lower left hand particle. The sensitivity to specific atomic column features would explain why the network failed to identify these regions. This would also explain why, in the case of the Au nanoparticles, the network was unable to generalize to segment the CdSe micrographs. We hypothesize that the introduction of a combined dataset forced the network to learn a wider number of atomic column representations and therefore improved performance on less represented regions in any one dataset.

These findings suggest that the path to high performance, automated, and generalizable segmentation, based on the current architecture, is to provide a diverse dataset for neural network training. Improved performance could likely be achieved in one of two ways: first, as stated before, creating a network based on a diverse dataset representing most atomic lattice contrast scenarios. This clearly presents challenges in terms of acquiring such a dataset. The second path forward would be to develop a neural network architecture which would learn more textural information, for instance learning rows of atomic columns as opposed to individual columns. Already work has been done which has shown that less data is required to train networks which limit their kernels to spherical harmonics because of the introduced rotational invariance [34]. If a similar approach could be taken in

order to favor learning textures, performance could also potentially improve.

The results presented show the potential for developing automated characterization. We have been able to train the U-Net architecture to segment images for materials with variable scattering factors. Automated segmentation, such as this, could then be used as a base for further automated classification of local atomic structures, including defects. Ultimately, statistics based on these classifications of local atomic structures could be used to help enhance prediction of material structures and the influence of local structural heterogeneity on properties and performance.

#### IV. CONCLUSION

Segmentation using neural networks on HRTEM images which include a crystalline region and amorphous background is a new area of exploration. This method could have impact on high throughput materials characterization in the HRTEM. We have shown that a U-Net architecture can achieve state-of-the-art segmentation results on HRTEM images. Segmentation using U-Net appears to depend strongly on learning atomic column representations. We have also determined that accurate location of particles is not dependent on mass thickness contrast but instead on the presence of atomic columns, which is promising for the application to low atomic number materials. We have also found that training on a diverse set of materials leads to the most generalizable neural network, as well as overall enhanced accuracy across the test set. Additionally, the developed neural network is able to outperform traditional segmentation techniques such as Bragg peak filtering on low atomic number materials by a fairly significant margin. We have also demonstrated the possibility of a high throughput characterization pipeline using HRTEM. While this study was not high throughput, each individual part used automated techniques from synthesis, to imaging, and finally segmentation. This technique demonstrates the potential of CNNs as the base for further analysis and classification tools for local atomic structure.

#### V. DATA AVAILABILITY

The complete workflow for micrograph preprocessing, network training, and testing is available in Jupyter notebooks at <https://github.com/ScottLabUCB/HTTEM/tree/master/pyNanoFind>

#### VI. ACKNOWLEDGEMENTS

Work at the Molecular Foundry was supported by the Office of Science, Office of Basic Energy Sciences, off the U.S. Department of Energy under Contract No. DE-AC02-05CH11231. This material is based upon work supported by the National Science Foundation Graduate Research Fellowship under Grant No. DGE-1752814. This work was also supported by National Science Foundation STROBE grant DMR-1548924. CdSe synthesis was supported by the Department of Energy, Office of Energy Efficiency and Renewable Energy (EERE), under Award Number DE-EE0007628. The authors would like to thank Haoran Yang and Emory Chan for providing the CdSe nanoparticles. The authors would also like to thank Colin Ophus, Mike MacNeil, and Tess Smidt for their feedback and comments during the writing of this manuscript.

#### VII. AUTHOR CONTRIBUTIONS

M.C.S. and C.K.G. conceived the project and designed the experiments. C.K.G. and C.G. optimized the network architecture. C.K.G. acquired the training images, trained the network, and tested the network. C.K.G. and M.C.S. wrote the manuscript. All authors discussed the results and commented on the manuscript.

#### VIII. COMPETING INTERESTS

The authors declare no competing financial or non-financial interests.

- 
- [1] Jain, A. *et al.* Commentary: The materials project: A materials genome approach to accelerating materials innovation. *APL Materials* **1**, 011002 (2013).
  - [2] Needs, R. J. & Pickard, C. J. Perspective: Role of structure prediction in materials discovery and design. *APL Materials* **4**, 053210 (2016).
  - [3] Hattrick-Simpers, J. R., Gregoire, J. M. & Kusne, A. G. Perspective: Composition-structure-property mapping in high-throughput experiments: Turning data into knowledge. *APL Materials* **4**, 053211 (2016).
  - [4] Tabor, D. P. *et al.* Accelerating the discovery of materials for clean energy in the era of smart automation. *Nature Reviews Materials* **3**, 5–20 (2018).
  - [5] Chan, E. M. *et al.* Reproducible, high-throughput synthesis of colloidal nanocrystals for optimization in multidimensional parameter space. *Nano Letters* **10**, 1874–1885 (2010).
  - [6] Zhao, S. *et al.* Influence of atomic-level morphology on catalysis: The case of sphere and rod-like gold nanoclusters for CO<sub>2</sub> electroreduction. *ACS Catalysis* **8**, 4996–5001 (2018).



- [7] Orfield, N. J., McBride, J. R., Keene, J. D., Davis, L. M. & Rosenthal, S. J. Correlation of atomic structure and photoluminescence of the same quantum dot: Pinpointing surface and internal defects that inhibit photoluminescence. *ACS Nano* **9**, 831–839 (2015).
- [8] Green, M. L. *et al.* Fulfilling the promise of the materials genome initiative with high-throughput experimental methodologies. *Applied Physics Reviews* **4**, 011105 (2017).
- [9] Rasool, H. I., Ophus, C., Klug, W. S., Zettl, A. & Gimzewski, J. K. Measurement of the intrinsic strength of crystalline and polycrystalline graphene. *Nature Communications* **4** (2013).
- [10] House, S. D., Chen, Y., Jin, R. & Yang, J. C. High-throughput, semi-automated quantitative STEM mass measurement of supported metal nanoparticles using a conventional TEM/STEM. *Ultramicroscopy* **182**, 145–155 (2017).
- [11] Ophus, C., Shekhawat, A., Rasool, H. & Zettl, A. Large-scale experimental and theoretical study of graphene grain boundary structures. *Physical Review B* **92** (2015).
- [12] Laramy, C. R., Brown, K. A., O'Brien, M. N. & Mirkin, C. A. High-throughput, algorithmic determination of nanoparticle structure from electron microscopy images. *ACS Nano* **9**, 12488–12495 (2015).
- [13] Szegedy, C., Toshev, A. & Erhan, D. Deep neural networks for object detection. In Burges, C. J. C., Bottou, L., Welling, M., Ghahramani, Z. & Weinberger, K. Q. (eds.) *Advances in Neural Information Processing Systems 26*, 2553–2561 (Curran Associates, Inc., 2013).
- [14] Ronneberger, O., Fischer, P. & Brox, T. U-net: Convolutional networks for biomedical image segmentation. In Navab, N., Hornegger, J., Wells, W. M. & Frangi, A. F. (eds.) *Medical Image Computing and Computer-Assisted Intervention – MICCAI 2015*, vol. 9351, 234–241 (Springer International Publishing, 2015).
- [15] Nicholson, W. V. & Glaeser, R. M. Review: Automatic particle detection in electron microscopy. *Journal of Structural Biology* **133**, 90–101 (2001).
- [16] Wang, F. *et al.* DeepPicker: A deep learning approach for fully automated particle picking in cryo-EM. *Journal of Structural Biology* **195**, 325–336 (2016).
- [17] Fultz, B. & Howe, J. *Transmission Electron Microscopy and Diffractometry of Materials* (Springer Berlin Heidelberg, 2013).
- [18] Ziatdinov, M. *et al.* Deep learning of atomically resolved scanning transmission electron microscopy images: Chemical identification and tracking local transformations. *ACS Nano* **11**, 12742–12752 (2017).
- [19] Madsen, J. *et al.* A deep learning approach to identify local structures in atomic-resolution transmission electron microscopy images. *Advanced Theory and Simulations* **1**, 1800037 (2018).
- [20] Ziatdinov, M. A., Dyck, O., Jesse, S. & Kalinin, S. V. Atomic mechanisms for the Si atom dynamics in graphene: chemical transformations at the edge and in the bulk (2019).
- [21] Maksov, A. *et al.* Deep learning analysis of defect and phase evolution during electron beam-induced transformations in WS<sub>2</sub>. *npj Computational Materials* **5**, 12 (2019).
- [22] Schiøtz, J. *et al.* Identifying atoms in high resolution transmission electron micrographs using a deep convolutional neural net. *Microscopy and Microanalysis* **24**, 512–513 (2018).
- [23] Schiøtz, J. *et al.* Using neural networks to identify atoms in hrtem images. *Microscopy and Microanalysis* **25**, 216–217 (2019).
- [24] Kalinin, S. V. *et al.* Lab on a beam—big data and artificial intelligence in scanning transmission electron microscopy. *MRS Bulletin* **44**, 565–575 (2019).
- [25] Groom, D. J. *et al.* Automatic segmentation of inorganic nanoparticles in BF TEM micrographs. *Ultramicroscopy* **194**, 25–34 (2018).
- [26] Get started with the image labeler - MATLAB & Simulink. URL <https://www.mathworks.com/help/vision/ug/get-started-with-the-image-labeler.html>.
- [27] Schorb, M., Haberbosch, I., Hagen, W. J. H., Schwab, Y. & Mastronarde, D. N. Software tools for automated transmission electron microscopy. *Nature Methods* (2019).
- [28] Lim, B., Xiong, Y. & Xia, Y. A water-based synthesis of octahedral, decahedral, and icosahedral Pd nanocrystals. *Angewandte Chemie International Edition* **46**, 9279–9282 (2007).
- [29] F. Niekel, C. O. T. P., P. Ercius. openNCEM (2016–). URL <https://openncem.readthedocs.io/en/latest/>.
- [30] Geron, Aurelien. *Hands-On Machine Learning with Scikit-Learn & TensorFlow* (O'Reilly Media, 2017), 1 edn.
- [31] Chollet, F. Keras (2015–2019). URL <https://keras.io/>.
- [32] Goodfellow, I., Bengio, Y. & Courville, A. *Deep Learning* (MIT Press, 2016). <http://www.deeplearningbook.org>.
- [33] Kingma, D. P. & Ba, J. L. Adam: A Method for Stochastic Optimization. *arXiv* 1–15 (2015). arXiv:1412.6980v9.
- [34] Worrall, D. E., Garbin, S. J., Turmukhambetov, D. & Brostow, G. J. Harmonic networks: Deep translation and rotation equivariance. *CoRR* abs/1612.04642 (2016). 1612.04642.